Microstructure and Mechanical Behavior of Polyamide 66-Precipitated Calcium Carbonate Composites: Influence of the Particle Surface Treatment

J. Cayer-Barrioz,[1] L. Ferry,[2] D. Frihi,[3] K. Cavalier,[4] R. Séguéla,[1] G. Vigier[1]

[1]*Groupe d'Etudes de Métallurgie Physique et de Physique des Matériaux, INSA de Lyon, Bâtiment Blaise Pascal, 69621 Villeurbanne, France*
[2]*Centre des Matériaux de Grande Diffusion, Ecole des Mines, 30319 Alès, France*
[3]*Laboratoire d'Analyse Industrielle et de Génie des Matériaux, Université du 08 mai 1945, 24000 Guelma, Algérie*
[4]*Solvay Specialités France, Route d'Arles, 13129 Salin de Giraud, France*

Received 24 November 2004; accepted 10 June 2005
DOI 10.1002/app.22826
Published online 12 January 2006 in Wiley InterScience (www.interscience.wiley.com).

ABSTRACT: The effects of interfacial adhesion strength on the mechanical behavior of composites of polyamide 66 and precipitated calcium carbonate ($CaCO_3$) particles have been investigated. The 50 nm average diameter particles have been surface-treated using two kinds of coupling agent having various affinities with respect to the matrix. The surface-modified particles have been incorporated into the polyamide matrix via melt processing. Tensile and impact tests, associated with dynamical mechanical analysis, have been performed on injection-molded samples. The structural characterization of the specimens has been carried out using differential scanning calorimetry and wide-angle X-ray scattering. It is observed that the matrix structure is roughly insensitive to the surface treatment, despite a weak nucleating effect of the filler particles. In contrast, the particle surface treatment strongly influences the particle dispersion in the polymer matrix. Although dispersion was not optimized, the elastic properties of the reinforced polyamide increase with the $CaCO_3$ content, below as well as above the glass transition temperature. Impact toughness decreases for $CaCO_3$ weight fraction greater than 5%. Scanning electron microscopy investigation reveals that the interfacial adhesion affects local deformation processes, such as debonding and fibrillation of the polymer matrix around the particles, during the macroscopic deformation of the composites. J Appl Polym Sci 100: 989–999, 2006

Key words: functional filler particles; precipitated calcium carbonate; $CaCO_3$; interfacial adhesion strength; polyamide 66

INTRODUCTION

Although cost reduction has been the most common purpose for adding mineral fillers to polymers, fillers are also used for improving stiffness and dimensional stability.[1–3] Calcium carbonate ($CaCO_3$) is one of the most usual mineral filler used in semicrystalline polymers and generally has a micrometric size.

A number of studies has been devoted to the influence of the morphological changes on the mechanical properties on $CaCO_3$-filled polymers. For instance, in the case of polypropylene that crystallizes into several forms, the addition of fillers can promote polymorphism, which improves mechanical performances.[4] Crystallinity and crystallite size can also be changed. Moreover, changes in the matrix morphology, such as transcrystallinity and crystalline texture, can be induced by the presence of fillers.[3,5] Consequently, the actual origin of the toughening effect of fillers in polymeric matrices is not well understood.

The mechanical behavior of the polymer is also likely to be modified via the interfacial properties between the filler and the matrix. In recent years, several authors have investigated the role of interfacial adhesion between filler and matrix on the resulting mechanical properties of composites based on polypropylene or polyethylene. However, little has been reported in the case of polyamides. The interface has been shown to play a key role, since it determines the stress transfer between the matrix and the particles and affects the local processes occurring during macroscopic deformation of the composites, in particular, the debonding process.[6] The particle-matrix interaction is also expected to influence the filler particle dispersion in the matrix and the crystalline morphology around the particles.

The polymer-particle interface can be modified by functional treatment of the particle surface to make it more or less compatible with the polymer matrix. The functional treatment can be classified into two broad categories: nonreactive treatment and reactive treatment.[7–9] The interaction between the inorganic surface

Correspondence to: G. Vigier (Gerard.Vigier@insa-lyon.fr).
Contract grant sponsor: Solvay Spécialités France.

and the polymer matrix can be tuned by selecting appropriate endgroups.[6] It is also noteworthy that decreasing the particle size at constant weight fraction allows increasing the influence of the interface via the increase of specific surface area.

This paper focuses on the study of composites of polyamide 66 (PA66) with surface-modified precipitated $CaCO_3$ particles of average diameter 50 nm. PA66 exhibits excellent thermomechanical behavior, but is highly sensitive to water absorption.[10–12] For that reason, the environment has been accurately controlled during this work. To investigate the particle-matrix adhesion, and its role on the local deformation processes, two surface treatments having different affinities with respect to the matrix have been studied. Uncoated $CaCO_3$ particles have also been investigated for comparison. PA66 is well known to crystallize into a single form[13] and is therefore less likely to present filler-induced structural modifications.

EXPERIMENTAL

Materials

The polymer used in this study is a PA66 supplied by Rhodia under the trade name Technyl A216. The filler consists of precipitated $CaCO_3$ powders manufactured by Solvay, with a particle mean size of 50 nm. The filler weight fraction span the range 3–20%. The $CaCO_3$ particles are coated either with stearic acid (AST) as nonreactive treatment with respect to the PA66 matrix, or with an amino acid (AA) agent having 10 carbon aliphatic chain as reactive treatment. Both coupling agents have been added in the amount of 3 wt % with respect to the filler. Uncoated precipitated $CaCO_3$ is also used for comparison.

PA66 has been first compounded with $CaCO_3$ particles in desired proportions, using a single screw extruder. The resulting pellets have been injected-molded into dog bone-shaped tensile bars 4 mm thick and 10 mm large, with a sample gauge length of 110 mm. Unfilled PA66 samples have been also prepared for comparison. Table I reports the characteristics of all the composites. Their denomination reads as follows: PA66-AST5 means that PA66 was filled with 5% of AST-treated $CaCO_3$. This series of samples allow studying both the influence of increasing $CaCO_3$ content as well as the interfacial adhesion strength.

Previous studies[10–12] have demonstrated the strong sensitivity of the mechanical properties of polyamide materials to water absorption. The plasticization of the polyamide amorphous phase by water is known to induce a very substantial decrease in elastic properties and an improvement of the plastic properties. To reduce the effects of variable moisture on the mechanical behavior, the specimens have been systematically stored in a dried state immediately after processing.

TABLE I
Material Properties

Sample code	$CaCO_3$ content (wt %)	Particle mean size (nm)	Surface treatment (wt %)
PA66	0		No
PA66–5	5	50	No
PA66–10	10	50	No
PA66–20	20	50	No
PA66-AST3	3	50	3% stearic acid
PA66-AST5	5	50	3% stearic acid
PA66-AST10	10	50	3% stearic acid
PA66-AST20	20	50	3% stearic acid
PA66-AA5	5	50	3% amino acid
PA66-AA20	20	50	3% amino acid

Physical and mechanical measurements

The techniques used to characterize the composite samples include differential scanning calorimetry (DSC), wide-angle X-ray scattering (WAXS), tensile testing, dynamical mechanical analysis (DMA), impact tests, and scanning electron microscopy (SEM).

DSC measurements have been carried out on a Perkin–Elmer DSC7, both upon heating and cooling, at a scanning rate of 10 K/min, in the temperature range 293–553 K. The temperature and heat flow scales have been calibrated from the melting scans of high purity indium and zinc samples, at the same heating rate. For determining the crystallinity of the PA66 component in the composites, a value of 200 $\pm$ 10 J/g has been used for the heat of fusion of 100% crystalline PA66.[14] All the data are average values of two measurements. Verification has been made in the case of neat PA66, that injection-molded samples are fairly homogeneous throughout their length, regarding the DSC measurements. The accuracy of the data is about 2% regarding the crystallinity, and $\pm$1 K for the melting and crystallization temperatures.

WAXS has been performed in transmission mode using the monochromated CuK_α radiation from a Rigaku rotating anode generator operated at 40 kV and 28 mA. The samples were machined out from the tensile bars to investigate separately the core and the 1-mm thick skin of these injection-molded samples.

The tensile properties of the dog bone-shaped specimens have been studied at room temperature and at 353 K, using a MTS 1-ME tensile testing machine. Considering that the glass transition temperature of PA66 is about 320 K,[15] the amorphous phase of PA66 is rubbery for the experiments carried out at 353 K. The tests have been performed at a crosshead speed of 100 mm/min, which means an initial strain rate of 1.52×10^{-2} s^{-1}. The reported data are average values of five measurements at room temperature and three measurements at 353 K.

DMA have been carried out on a home-built torsion pendulum[16] operating under helium at a frequency of

0.1 Hz. The temperature domain 220–500 K has been scanned at a heating rate of 1 K/min. The storage modulus, G', and the loss modulus, G'', have been computed from integrations of the stress and strain functions. The loss factor, tan δ, is defined as the ratio G''/G'. The samples were cut in the form of rectangular bars 1 mm thick, 2 mm wide, and 25 mm long.

The toughness of the materials has been determined using an instrumented Charpy-type impact tester[17] with a maximum energy of 4 J, with an impact speed of 2.9 m/s. The sample dimensions were 4 mm × 10 mm × 60 mm. All the reported data are average values of 10 measurements at room temperature.

SEM observations have been performed on a JEOL 840 ALGS SEM operated at 10 kV. The postmortem fracture surfaces of samples broken under tensile loading were gold-coated prior to examination. For a better insight into the filler-matrix interfacial region, uncoated fracture surfaces have been studied by means of an environmental scanning electron microscope, FEI XL30 ESEM FEG, operating at a very low accelerating voltage of 0.8 kV.

RESULTS

Thermal analysis

To study the influence of the precipitated $CaCO_3$ on the crystallization mechanism of the PA66 matrix, DSC studies of nonisothermal crystallization and melting have been carried out. The onset temperature and peak temperature of both the melting and crystallization peaks have been determined, together with the crystallinity of the PA66 matrix in the composites. Figure 1 reports the whole data, using the same labels as in Table I. Only little modification is observed in the melting temperature (Fig. 1(a)) with the presence of fillers: both the peak melting temperature and the onset fluctuate about the corresponding value of neat PA66. Figure 1(b) shows that $CaCO_3$ particles also have a very weak influence on the nucleation of PA66, independently of the coupling agent; indeed, the crystallization onset slightly increases with addition of $CaCO_3$. The crystallization data of Figure 1(c) exhibit no major effect of the filler, except for the PA66–20 sample. It can be concluded from this thermal analysis that the development of the crystalline phase of the PA66 matrix is not affected by the presence of precipitated $CaCO_3$, irrespective of both the amount of filler and the surface treatment.

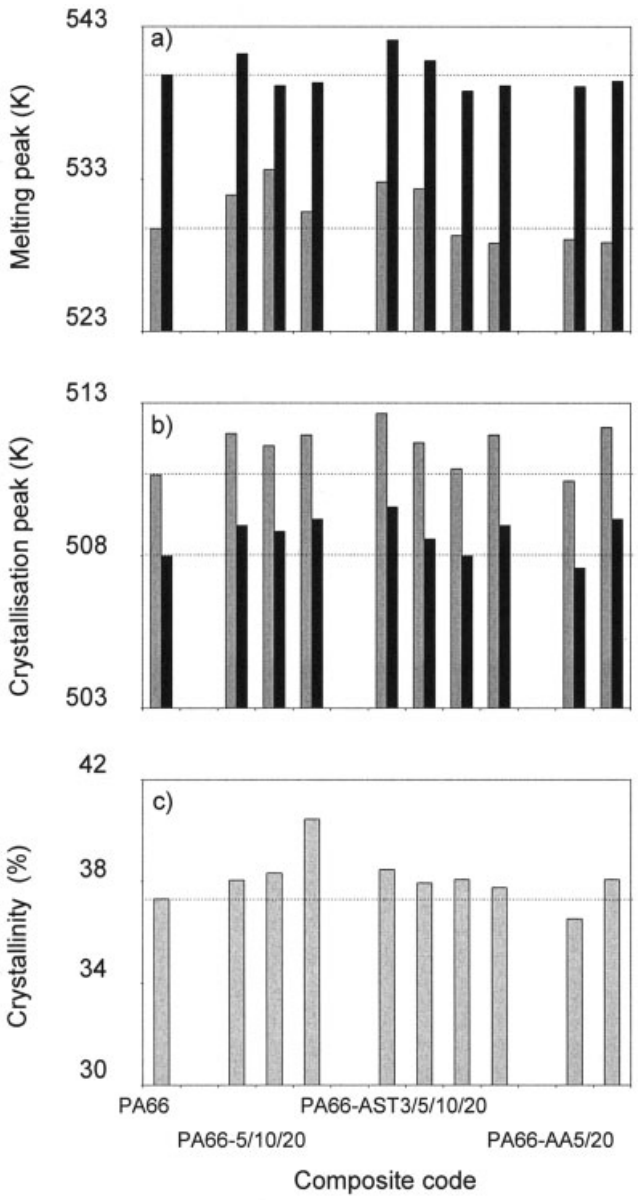

Figure 1 DSC data for temperatures of (a) melting peaks, (b) crystallization peaks, and (c) the crystallinity of PA66 determined from the melting scan. Light gray bars show the onset, while dark gray bars give the temperature at peak, for both melting and crystallization. The sample codes refer to the composites of Table I. For an easier comparison, the horizontal dotted lines indicate the corresponding data of neat PA66 throughout the graph for every parameter.

Crystal structure of the composites

The WAXS patterns of all the samples reported show the two strong (100) and (010, 110) reflections characteristic of α-phase crystals of PA66.[13] This is illustrated in Figures 2(a) and 2(b) for the neat PA66 and PA66-AST5 samples, respectively. The uniform intensity of the two reflections reveals the absence of injection-induced texture. The relative intensity of the two reflections remains constant for all the samples and is about that observed for isotropic PA66,[18] as shown in the WAXS intensity profiles Figure 2(c) for neat PA66 and PA66-AST5. This observation, which holds for all the samples, is consistent with an isotropic material with no injection-induced texturing. Finally, considering that the scattering peak width is similar for all the

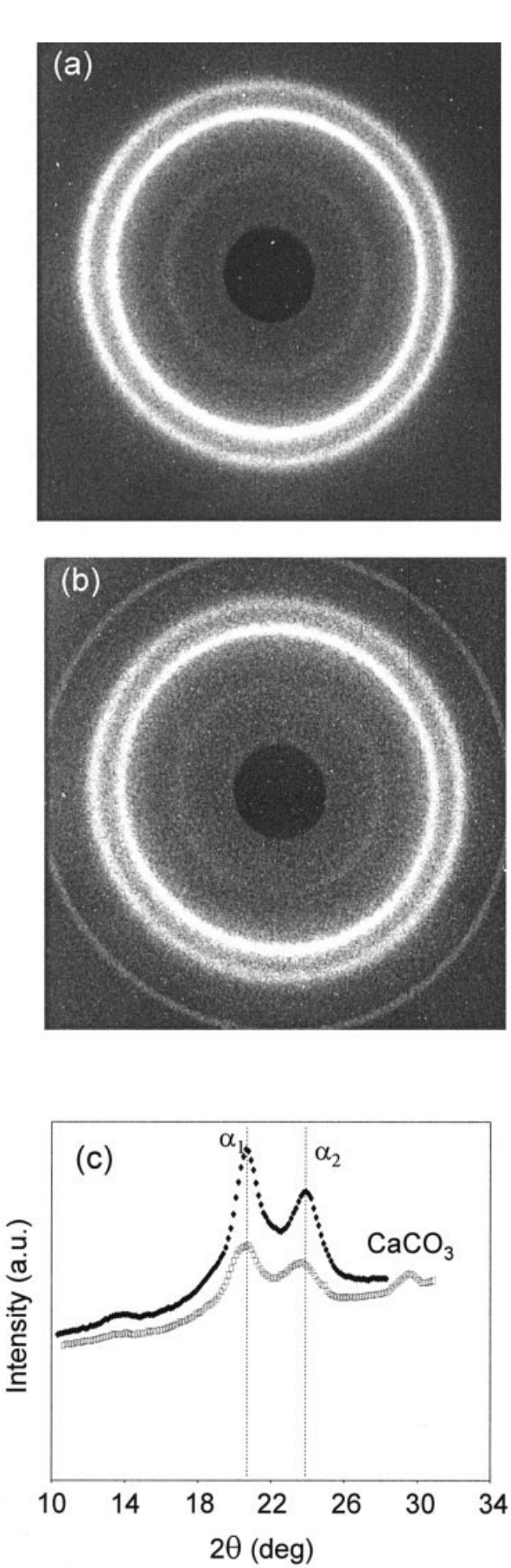

Figure 2 WAXS diffraction patterns of (a) unfilled PA66, (b) PA66-AST5, and (c) intensity profiles for neat PA66 (♦) and PA66-AST5 (□).

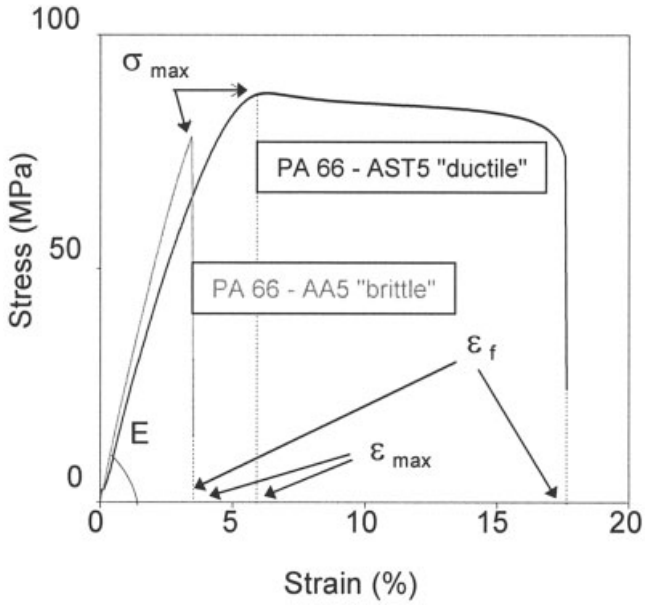

Figure 3 Typical stress–strain curves for PA66-AST5 and PA66-AA5 showing ductile and brittle behavior.

composites studied, it is concluded that the crystal size is roughly identical, irrespective of the surface treatment.

The same observations have been made between the core and the skin for every composite, revealing no significant structural modification throughout the sample thickness.

Tensile properties

Ductile as well as brittle failure has been observed at room temperature, as illustrated on the engineering stress–strain curves of Figure 3 for the PA66-AST5 and PA66-AA5 samples. The Young's modulus, the maximal stress, the corresponding strain, and the failure strain are reported in Table II for all the materials studied. The Young's modulus of the composites increases with increasing $CaCO_3$ content, notably in the case of AST and AA-treated fillers. However, a drop in Young's modulus is observed for the low $CaCO_3$ content composites with regard to neat PA66, notably for untreated filler**.** This softening effect cannot be due to crystallinity or texture modifications, as shown earlier. However, the poor adhesion of the $CaCO_3$ particles to the PA66 matrix can be responsible for premature debonding at some particle-matrix interfaces, upon loading. Unavoidable injection-molding defects are the locus of stress concentrations that may promote

TABLE II
Mechanical Properties of the Composites

Sample	Mechanical behavior	E (MPa)	σ_{max} (MPa)	ε_{max} (%)	ε_f (%)
PA66	Mixed	2300 ± 30	85 ± 3	5.7 ± 0.7	6.0 ± 1.0
PA66–5	Brittle	2000 ± 50	64 ± 5	3.6 ± 0.4	3.6 ± 0.4
PA66–10	Brittle	2250 ± 80	57 ± 8	3.0 ± 0.5	3.0 ± 0.5
PA66–20	Brittle	2100 ± 40	60 ± 5	3.1 ± 0.3	3.1 ± 0.3
PA66-AST3	Ductile	2160 ± 80	84 ± 8	6.2 ± 1.2	19 ± 8
PA66-AST5	Ductile	2500 ± 120	86 ± 2	6.5 ± 0.5	13 ± 9
PA66-AST10	Brittle	3080 ± 50	65 ± 6	2.7 ± 0.3	2.7 ± 0.3
PA66-AST20	Brittle	3120 ± 80	56 ± 5	2.2 ± 0.3	2.2 ± 0.2
PA66-AA5	Brittle	2630 ± 60	73 ± 9	3.9 ± 0.9	3.9 ± 0.9
PA66-AA20	Brittle	3220 ± 20	65 ± 6	2.7 ± 0.3	2.7 ± 0.3

E, Young's modulus; σ_{max}, maximal stress; ε_{max}, corresponding strain; and ε_f, failure strain (strain rate = 1.52×10^{-2} s^{-1}; temperature 296 K).

such premature debonding. For filler contents greater than 5%, the stiffening effect of the filler counterbalances the negative effect of premature debonding. The systematic debonding of the matrix from the filler will be discussed in more details in the "Discussion" section.

For 5% of $CaCO_3$, the influence of the surface treatment is clearly observed as the Young's modulus follows the ranking

$$E(PA66\text{–}5) < E(PA66\text{-}AST5) < E(PA66\text{-}AA5) \quad (1)$$

As a matter of fact, increasing adhesion involves a stiffness increase, which corroborates the aforementioned conclusion that premature interfacial debonding has a negative role on stiffness.

The maximal stress and its corresponding strain increase with increasing $CaCO_3$ content in the case of AST and AA treatments. Untreated $CaCO_3$ composites display a strong drop of these properties with respect to neat PA66 but little sensitivity to filler content. The elongation at break of the composites decreases in comparison with neat PA66, except for the case of PA66-AST at low filler content that will be discussed later. On the surface of brittle fracture, large aggregates of $CaCO_3$ have always been observed, as illustrated Figure 4. The probability to encounter such aggregates increases with increasing $CaCO_3$ weight fraction. Similar observations have already been reported by Bartczak et al. in the case of $CaCO_3$-filled high-density polyethylene[1] and by Wilbrink et al. in the case of $CaCO_3$-filled polyamide 6.[19] Decreasing the size of the filler particles is expected to reduce the occurrence of such aggregates, provided that melt-processing is efficient enough.

In contrast to room temperature, tensile tests performed at 353 K on neat PA66 and on the 5% composites systematically displayed a ductile behavior. The data of Table III show that the stress level at the yield point, σ_{max}, decreases significantly as compared with that at room temperature, whereas the elongation at failure, ε_f, increases far beyond the corresponding value at room temperature.

Young's moduli at 353 K are much smaller than at room temperature (Table III), because of the fact that the PA66 amorphous phase is rubbery at that temperature. Notwithstanding, a stringent 2.5-fold increase of Young's modulus is observed at 353 K for the 5% $CaCO_3$ composite as compared with unfilled PA66. This is consistent with previous observations reported for nylon6/clay nanocomposites above the glass transition of the matrix, with clay contents in the range 3–5%.[20,21] In that case, it has been pointed out that the experimental modulus data were significantly higher

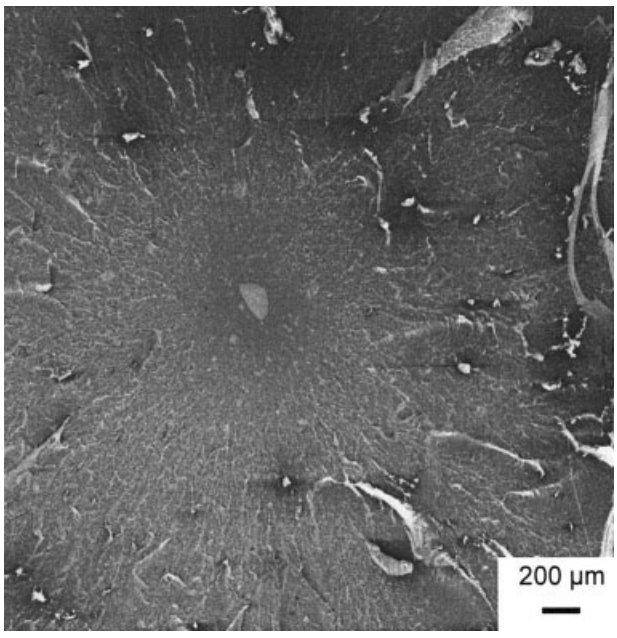

Figure 4 SEM micrograph of a broken PA66-AST20 tensile sample showing a $CaCO_3$ aggregate at the origin of the brittle fracture.

TABLE III
Mechanical Properties of the 5% $CaCO_3$ Composites at 1.52×10^{-2} s^{-1} and 353 K

Sample	Mechanical behavior	E (MPa)	σ_{max} (MPa)	ε_{max} (%)	ε_f (%)
PA66	Ductile	440 ± 10	55 ± 2	20 ± 3	105 ± 54
PA66–5	Ductile	1640 ± 140	63 ± 5	12 ± 4	15 ± 6
PA66-AST5	Ductile	2000 ± 80	63 ± 2	13 ± 1	20 ± 4
PA66-AA5	Ductile	1470 ± 160	62 ± 6	16 ± 1	26 ± 1

E, Young's modulus; σ_{max}, maximal stress; ε_{max}, corresponding strain; and ε_f, failure strain are calculated as indicated in Figure 3.

than theoretical predictions from the common Kerner model.[21] This finding was ascribed to strong filler-matrix and filler–filler interactions.

Dynamic mechanical thermal analysis

Figure 5(a) shows the storage shear modulus variations with temperature of PA66 composites having various weight fractions of AST-coated $CaCO_3$. At 296 K, 20% of $CaCO_3$ induces a 16% increase in the shear modulus. The stiffness increase is more important at higher temperature, namely about 50% greater at 450 K. This confirms the previous observation on the Young's modulus computed from tensile testing. In contrast, the loss modulus data do not reveal reliable differences, which could result from the presence of fillers (Fig. 5(b)). Since the data are representative of the mechanical behavior of the amorphous component, this finding is in agreement with the absence of physical modifications of the amorphous phase. However, the G'' relaxation peak is shifted toward high temperature when adding $CaCO_3$ particles. As a consequence of the G' and G'' changes, the loss factor data, tan δ, reveals a decrease in the relative energy dissipated at the glass transition with the presence of filler (Fig. 5(c)). The shift of the tan δ peak to high temperature is also observed for tan δ as for G''.

The influence of the surface treatment on the mechanical behavior of the composites clearly appears through the G'' peak shift, namely +13 K for the AA treatment as compared with +6 K for the AST treatment.

Impact resistance

Figure 6 shows the impact resistance of every blends at room temperature. All the samples exhibit a brittle failure. From this figure, it can be seen that the fracture energy decreases with increasing filler content except for the PA66-AST5 sample. This behavior can be attributed to a poor dispersion of the $CaCO_3$ particles, as judged from the 300 μm aggregates that have systematically been observed at the locus of the fracture initiation.

Concerning the surface treatment effects, it can be seen from Figure 6 that the impact resistance for the 5% AST-treated composite is higher than that of the 5% AA-treated composite. Besides, the former composite is more impact resistant than neat PA66.

DISCUSSION

The influence of the filler content on the mechanical behavior of the composites is first discussed through the results of the AST-treated $CaCO_3$ PA66 composites. Then, the influence of the surface treatment on the interfacial adhesion strength is discussed on the basis of data from the 5% $CaCO_3$ composites.

Influence of the filler weight fraction

Using the tensile stress–strain experiments at room temperature, energies at break can be calculated from the area below the curve. The data are plotted in Figure 7 in the case of the AST-coated composites. A maximum energy is observed at ~17 MJ/m^3 for 3% of $CaCO_3$. As the weight fraction increases, the energy drops down to about 1 MJ/m^3 for 20% of filler. Energies at break greater than 10 MJ/m^3 correspond to a ductile behavior, whereas lower energies are relevant to a brittle failure.

The determining role of agglomerates in the failure process has been confirmed by SEM observations from broken samples under tensile testing. Figure 8(a) shows a SEM micrograph of a fracture surface from a PA66-AST3 sample with a fuzzy zone indicative of plastic processes. The fracture initiation looks like a crater surrounded by an elliptical zone with highly stretched ligaments, which suggest significant amount of energy dissipation (Fig. 8(b)). Outside the crater region, the sponge-like morphology of the fracture surface suggests that less plastic deformation is involved in the failure process, about 60 μm away from the fracture initiation locus. In contrast, Figure 8(c) shows the micrograph of PA66-AST10 fracture surface where a 300 μm wide $CaCO_3$ agglomerate can be seen as the origin of the brittle fracture.

Unfilled PA66 presents an intermediate response, *i.e.*, both brittle and ductile rupture has been observed

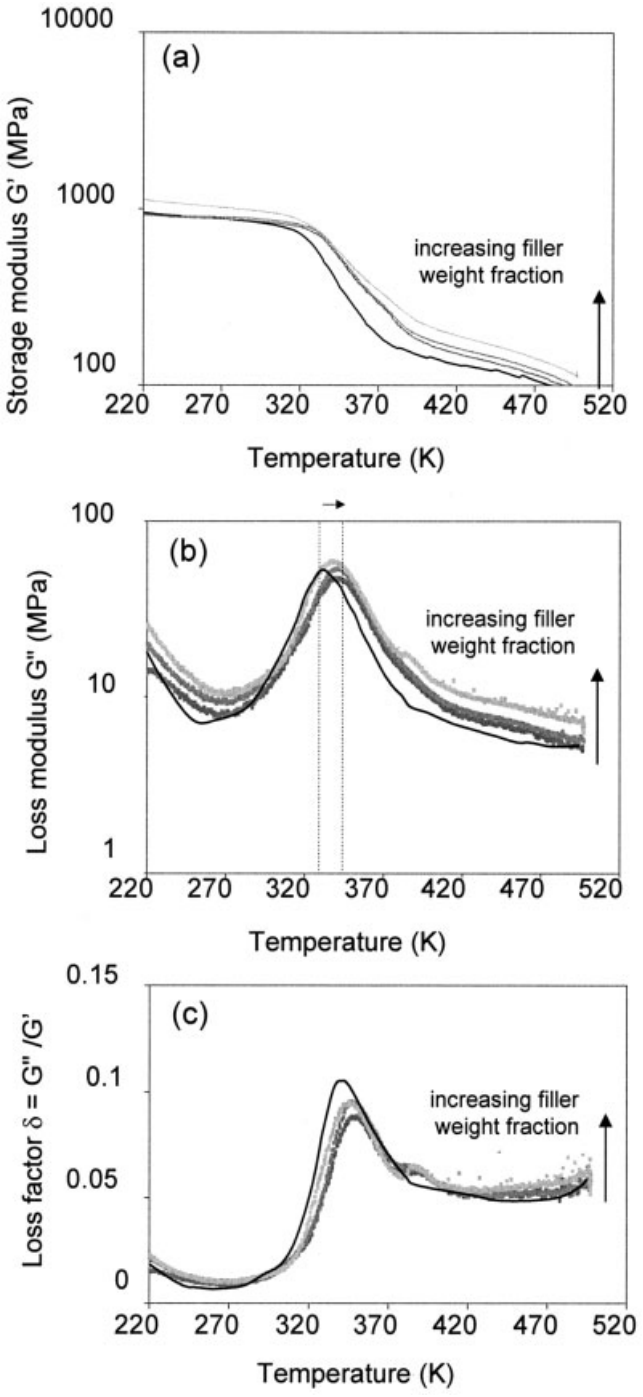

Figure 5 (a) Storage modulus (G'); (b) loss modulus (G''); and (c) loss factor (tan δ) versus temperature for composites having an increasing weight fraction of AST-coated fillers (the $CaCO_3$ weight fraction increases from 3, 5, 10 to 20% in the arrow direction).

statistically at room temperature. This is an indication that the ductile-to-brittle transition of neat PA66 is probably located about room temperature under these experimental conditions. The presence of casual structural defects originating from crystallization may turn failure either brittle or ductile depending whether the

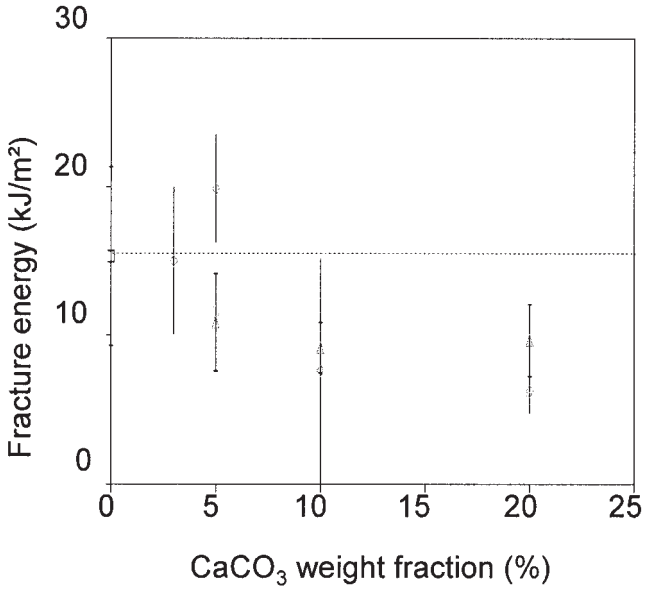

Figure 6 Fracture energy of the composites at room temperature as a function of the filler content: (□) unfilled, (Δ) untreated $CaCO_3$, (◇) AST-coated $CaCO_3$, and (○) AA-coated $CaCO_3$.

defect size is critical or not. The micrograph of Figure 8 (d) displays a fracture surface from a neat PA66 samples that failed in a brittle mode: the darker zone at the center of the star shape fracture initiation suggests such a structural defect.

The aforementioned findings give indication that the ductile-to-brittle transition of PA66 is shifted to lower temperature with the incorporation of $CaCO_3$. Similar results have previously been reported by several authors for various polymers composites.[22–24]

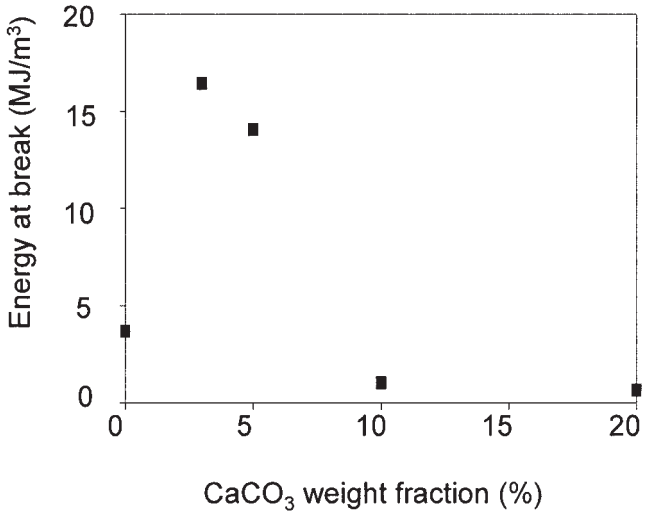

Figure 7 Energy at break as a function of the weight fraction of fillers for the PA66-AST composites, as computed from the tensile stress–strain curves at room temperature.

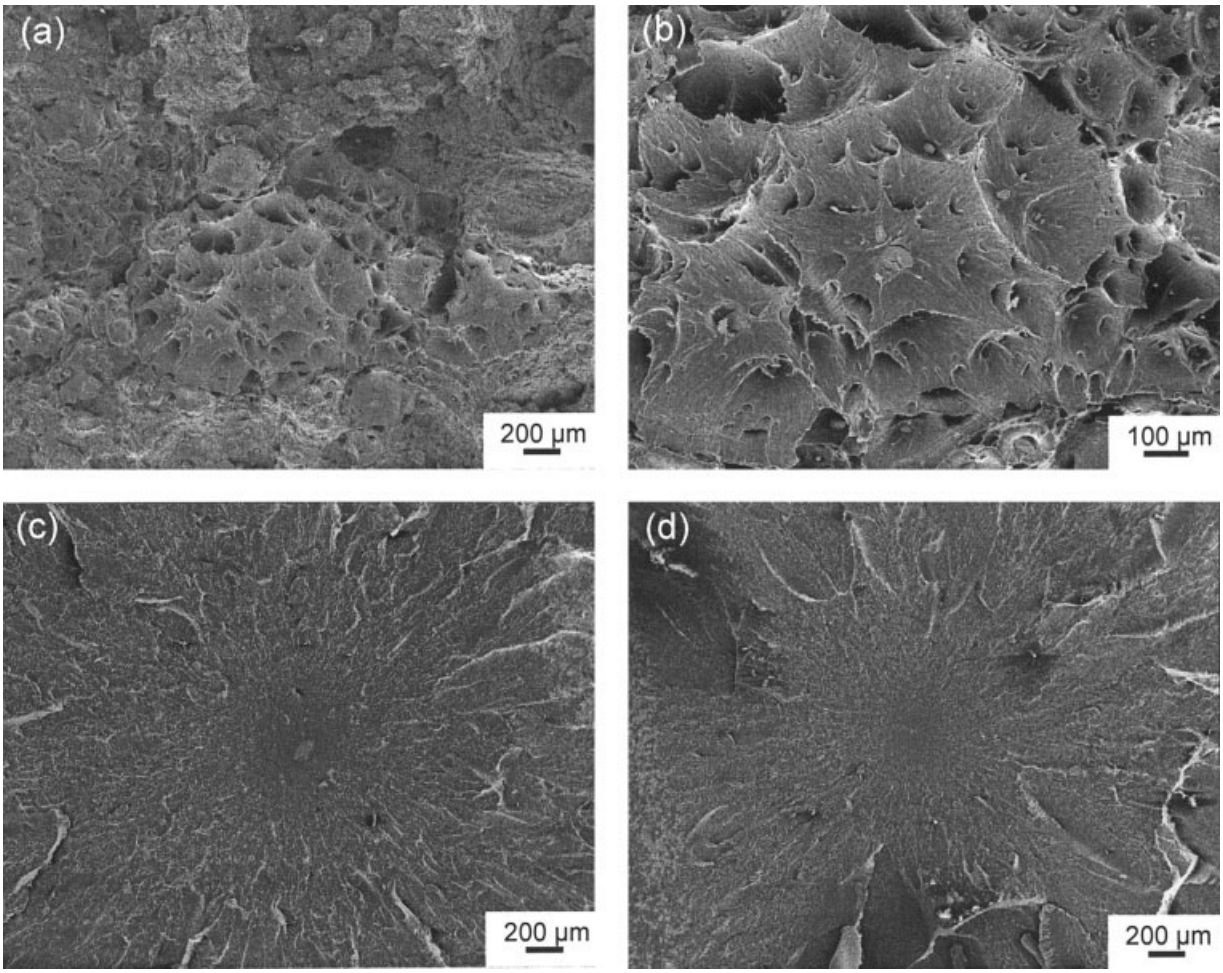

Figure 8 SEM micrographs of fracture surface of tensile samples: (a) PA66-AST3 and (b) enlarged detail from the central part of Figure 8(a); (c) PA66-AST10; and (d) unfilled PA66.

This transition can be attributed to a competition between brittle processes governed by microstructural flaws, and energy-absorbing plastic processes.[23] The incorporation of particles that can debond at the early stages of deformation makes the polymer matrix capable of undergoing large local plastic strains. The microfibrils that develop during plastic deformation of the matrix about the debonded particles are likely to both dissipate energy and prevent crack propagation.[22]

Indirect evidence of particle debonding can be obtained from a close examination of the initial part of the tensile stress–strain curves at room temperature. Figure 9 shows a clear departure from linearity well below the yield point for the two lowest filler weight fractions in the case of PA66-AST. This phenomenon is relevant to early anelastic events. According to Wilbrink et al.,[19] this is a piece of evidence of particle debonding from the matrix. This confirms that debonding of particles from the matrix has occurred before the yield point for PA66-AST3 and PA66-AST5. Above 10%, the dispersion of the fillers is so bad that

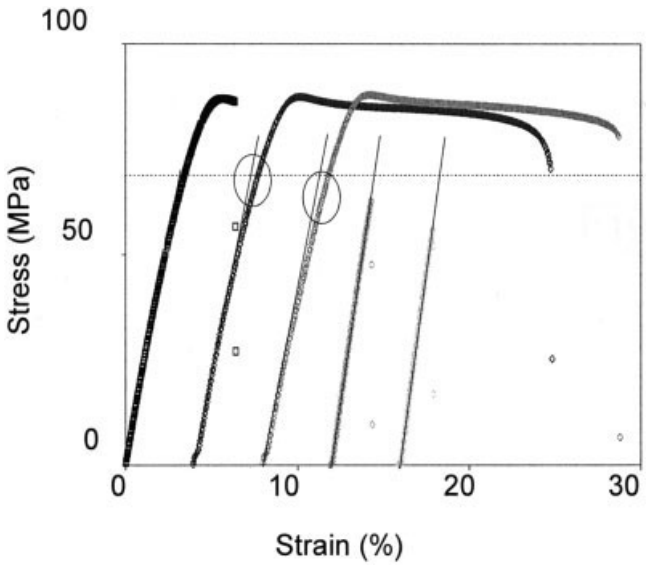

Figure 9 Stress–strain curves at room temperature of the PA66-AST composites (the $CaCO_3$ weight fraction increases from 0, 3, 5, 10 to 20%, from left to right; every curve is shifted by 20% along the strain axis for clarity).

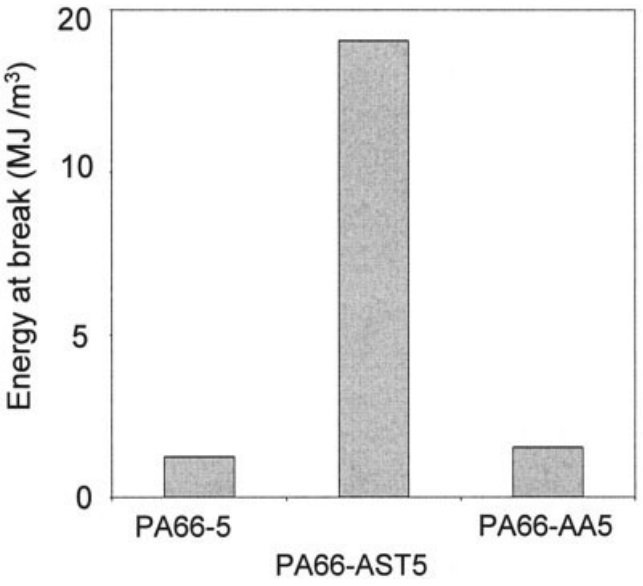

Figure 10 Energy at break as a function of the different surface treatment for the 5% $CaCO_3$ composites, as computed from integration of the tensile stress–strain curves at room temperature.

large agglomerates of fillers initiate brittle fracture (Fig. 9).

To sum up, the addition of fillers induces two opposing effects that modify the ductile-to-brittle transition of PA66:

- filler-matrix debonding that promotes local plastic processes and lowers the ductile to-brittle transition temperature,
- early initiation of cracks due to particle aggregates that shifts the transition to higher temperatures.

Role of the interfacial adhesion strength

The dynamic mechanical analysis has revealed a shift of the α relaxation peak with both AST and AA surface treatment of the $CaCO_3$ particles. Three hypotheses can be proposed for this phenomenon:

- A variation of the humidity of the samples. Considering that all the specimens have been stored in the same conditions prior to testing, and have been tested under the same experimental conditions, this hypothesis seems unlikely.
- A modification of the amorphous component mobility. However, the thermal analysis and the structural characterization indicate similar characteristics for the crystalline component of all the samples and the absence of texture. Therefore, there is no structural reason for the amorphous component to be physically different in the various composites.
- A purely mechanical effect. Considering the various degrees of matrix-particle adhesion, various degrees of stress transfer between the matrix and the filler is highly probable. The better particle-matrix adhesion in the case of AA treatment gives indeed the larger temperature shift of the α relaxation.

Energies at break calculated from the area below the stress–strain curves for the three kinds of composites having the same filler weight fraction, i.e., 5% of $CaCO_3$, are plotted in Figure 10. The PA66-AST5 sample exhibits the highest energy at break at $\sim$15 MJ/m^3 for ductile fracture. In contrast, the other two samples are brittle under the same experimental conditions. In the case of untreated $CaCO_3$, the poor dispersion capability of the filler is responsible for the occurrence of very large $CaCO_3$ clusters, up to 300 μm, which initiate the brittle fracture. Concerning the PA66-AST5 and PA66-AA5 samples, the size of the aggregates remains below 150 μm. Therefore, the large difference in the energies at break and failure mode may be attributed to the surface treatment, which governs the adhesion strength, and thus the debonding capabilities. As previously suggested by Thio et al.,[6] an estimation of the adhesion strength between the $CaCO_3$ fillers and the PA66 matrix can be obtained from the stress level at which debonding occurs (see Fig. 9), during tensile testing. Figure 11 shows the debonding stress of the 5% samples having different surface treatments, as determined from the deviation from linearity of the stress–strain curves. The higher debonding stress for the AA treatment is relevant to a stronger filler-matrix

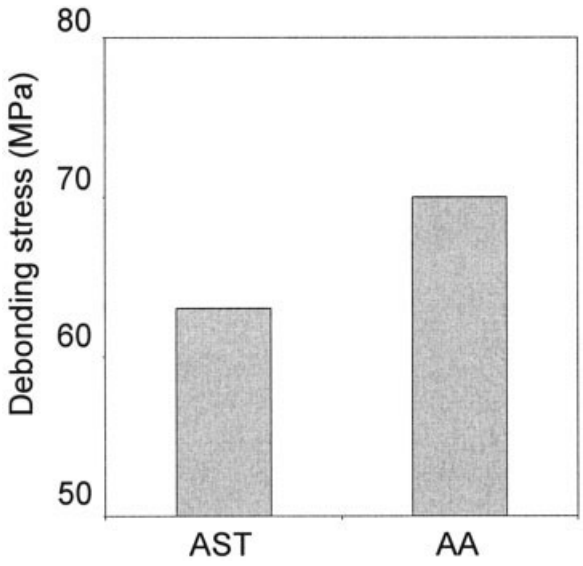

Figure 11 Macroscopic stress at the onset of debonding as a function of the surface treatment of the $CaCO_3$ particles.

adhesion, as compared with the AST treatment. The interfacial adhesion strength clearly appears to govern the mechanical behavior of the composites, since the composites with weaker interaction between filler and matrix exhibit higher toughness.

The nature of the particle-matrix interface has been confirmed by ESEM, which allows observations of fracture surfaces without metallic coating. The weak filler-matrix adhesion can be seen in Figure 12(a) in the case of untreated $CaCO_3$. In contrast, in the case of AST treatment of the $CaCO_3$ particles, Figure 12(b) shows that the interface between filler and matrix after failure is bridged by scarce fibrils. In the case of the AA treatment, Figure 12(c) reveals a stronger interaction between filler and matrix, as judged from the numerous and broad polymer bridges at the particle-matrix interface.

CONCLUSIONS

Adding precipitated $CaCO_3$ particles to PA66 have led to a composite with higher stiffness than the PA66 pure matrix, below as well as above the glass transition temperature. The matrix structure remained roughly insensitive to both surface treatment and filler content.

The micromechanism of reinforcement of the composites consists of

- debonding at the filler-matrix interface due to stress concentration in the rather soft PA66 matrix as compared with the $CaCO_3$ particles,
- local plastic deformation and fibrillation of the PA66 matrix about the particles, as a result of debonding.

The weaker the adhesion between the filler particles, the earlier was the debonding of the PA66 matrix. This caused greater plastic capabilities during deformation of the composites. A significant shift of the brittle-to-ductile transition at the macroscopic scale has been observed as a function of the interfacial adhesion strength.

The dispersion of the particles also proved to be critical for these composites. Filler agglomerates lead to reduced plastic capabilities. When large particle clusters are present, notably for untreated precipitated $CaCO_3$, voids rapidly turn into catastrophic cracks.

Even if the filler dispersion was not optimal to reach a strong reinforcement of PA66, the present investigation proved to be successful regarding the influence of the interfacial adhesion strength.

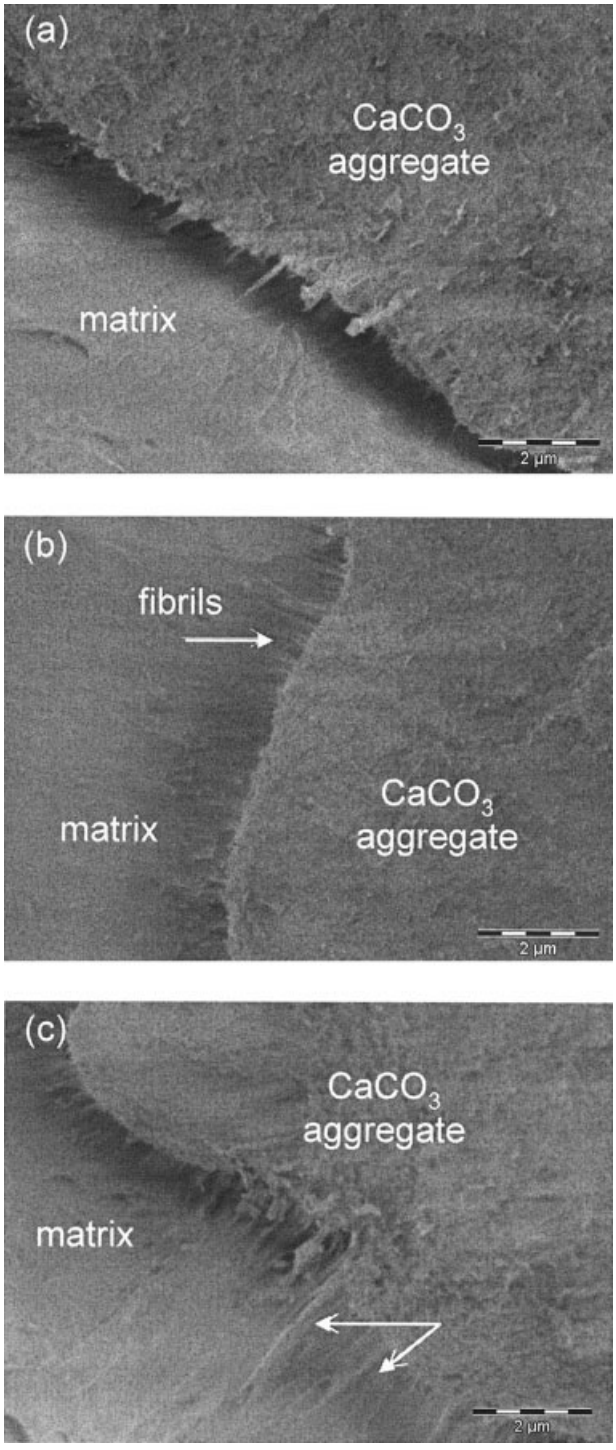

Figure 12 ESEM micrographs of the filler-matrix interface of the composites as a function of surface treatment: (a) untreated $CaCO_3$, (b) AST-coated $CaCO_3$, and (c) AA-coated $CaCO_3$.

Acknowledgments are addressed to G. Rodary and D. Sy (Solvay, Salin-de-Giraud) for their contribution to the partnership. The authors are also indebted to N. Issartel and H. Sautereau from the Laboratoire des Matériaux Macromoléculaires (INSA de Lyon, France) for assistance and helpful discussion on the impact tests, as well as to K. Masenelli-Varlot from the Groupe d'Etudes de Métallurgie Physique et de Physique des Matériaux (INSA de Lyon, France) for the ESEM observations. Rhodia Engineering Plastics is deeply acknowledged for providing the Technyl material.

References

1. Bartczak, Z.; Argon, A. S.; Cohen, R. E.; Weinberg, M. Polymer 1999, 40, 2347.
2. Plummer, C. J. G.; Mauger, M.; Béguelin, Ph.; Orange, G.; Varlet, J. Polymer 2004, 45, 1147.
3. Zuiderduin, W. C. J.; Westzaan, C.; Huétink, J.; Gaymans, R. J. Polymer 2003, 44, 261.
4. Labour, T.; Gauthier, C.; Séguéla, R.; Vigier, G.; Bomal, Y.; Orange, G. Polymer 2001, 42, 7127.
5. Muratoglu, O. K.; Argon, A. S.; Cohen, R. E.; Weinberg, M. Polymer 1995, 36, 921.
6. Thio, Y. S.; Argon, A. S.; Cohen, R. E. Polymer 2004, 45, 3139.
7. Demjén, Z.; Pukanszky, B.; Nagy, J. Composites A 1998, 29, 323.
8. Shui, M. Appl Surf Sci 2003, 220, 359.
9. Yang, R.; Liu, Y.; Wang, K.; Yu, J. J Anal Appl Pyrolysis 2003, 70, 413.
10. Hernandez, R. J.; Gavara, R. J Polym Sci Part B: Polym Phys 1994, 32, 2367.
11. Stuart, B.; Briscoe, B. J. Polym Int 1995, 38, 95.
12. Valentin, D.; Paray, F.; Guetta, B. J Mater Sci 1987, 22, 46.
13. Xenopoulos, A.; Clark, E. S. In Nylon Plastics Handbook; Kohan, M. I., Ed.; Hanser: Munich, 1995; Ch. 5.
14. Wunderlich, B. Macromolecular Physics, Vol. 3: Crystal Melting; Academic Press: New York, 1980.
15. Williams, J. C. L.; Watson, S. J.; Boydell, P. In Nylon Plastics Handbook; Kohan, M. I., Ed.; Hanser: Munich, 1995; Ch. 10.
16. Jourdan, C.; Cavaillé. J.-Y.; Perez, J. J Polym Sci Part B: Polym Phys 1989, 27, 2361.
17. Merle, G.; Yong-Sok, O.; Pillot, C.; Sautereau, H. Polym Test 1985, 5, 37.
18. Shen, L.; Phang, I. Y.; Chen, L.; Liu, T.; Zeng, K. Polymer 2004, 45, 3341.
19. Wilbrink, M. W. L.; Argon, A. S.; Cohen, R. E.; Weinberg, M. Polymer 2001, 42, 10155.
20. Lefebvre, J.-M. Encyclopaedia of Polymer Science and Technology; Kroschwitz, J., Ed.; Wiley: New York, 2002.
21. Chazeau, L.; Gauthier, C.; Vigier, V.; Cavaillé, J.-Y. Handbook of Organic-Inorganic Hybrid Materials and Nanocomposites, Vol. 1: Hybrid Materials; Nalwa, H. S., Ed.; American Scientific Publishers: Stevenson Ranch (CA), 2003; Ch. B.
22. Argon, A. S.; Cohen, R. E. Polymer 2003, 44, 6013.
23. Bartczak, Z.; Argon, A. S.; Cohen, R. E.; Weinberg, M. Polymer 1999, 40, 2331.
24. Thio, Y. S.; Argon, A. S.; Cohen, R. E.; Weinberg, M. Polymer 2002, 43, 3661.